ORIGINAL ARTICLE

Microstructure-based finite element modeling of a martensitic stainless steel during hot forging

Simin Dourandish[1] · Henri Champliaud[1] · Jean-Benoit Morin[2] · Mohammad Jahazi[1]

Abstract

This study aims to analyze material flow behavior and microstructure evolution during the hot deformation of a martensitic stainless steel with the view to simulating the open die forging process. For this purpose, hot compression tests were conducted using a Gleeble-3800 thermo-mechanical. A material model, based on the Arrhenius equation, was developed and implemented into the finite element simulation code Forge NxT 3.0® using a special user subroutine. Microstructure maps for the entire volume of the specimen were determined, and the occurrences of different softening phenomena were predicted as a function of hot deformation parameters. Good correlations were obtained between the simulation predictions and experimental results. The flow behavior of the material was also analyzed using the dynamic material model, and the unstable regions were identified. The obtained results were compared with the experimental and numerical simulation findings. The approach proposed in this paper, which integrates microstructure-based finite element simulation combined with a three-dimensional processing map, can be used for rapid and accurate optimization of the hot deformation process of martensitic stainless steels.

1 Introduction

Hot forging of large size ingots made of martensitic stainless steels (MSS) is a challenging processing step during the manufacturing of structural components that require high strength, high toughness, and good corrosion resistance such as valves, shafts, bearings, rotors, and bolting of gas turbine blades [1–3]. The main concern during the forging of these steels is the occurrence of large variations in the microstructure (e.g., austenite grain size) between the center and the surface of the forged part [4]. Such variations are at the source of cracking during the hot forging operation or can lead to unacceptable variations in properties in different regions of the final product.

The manufacturing process consists of alloy production in electric arc furnaces, followed by ingot casting and open die forging. During the latter step, the heterogeneous cast structure is broken down into a more refined microstructure and improved chemical homogeneity through the thickness of the large-size forged block [5–8]. The flow characteristic of a hot forging process consists of competing mechanisms of strain hardening, also called work hardening (WH), and softening phenomena such as dynamic recovery (DRV) and dynamic recrystallization (DRX). These mechanisms are affected by hot working parameters like temperature, strain, and strain rate [9–12]. So, optimizing these working parameters, related to metal forming, is of critical importance for the heavy forging industries, and therefore, the hot forging process should be designed carefully to obtain both the right shape and microstructure.

To accurately predict microstructure evolution and flow stress behavior during the ingot breakdown process at high temperatures, the development of reliable constitutive models is essential [13–15]. In this regard, isothermal hot

✉ Simin Dourandish
simin.dourandish.1@ens.etsmtl.ca

Mohammad Jahazi
mohammad.Jahazi@etsmtl.ca

[1] Department of Mechanical Engineering, École de Technologie Supériere, 1100 Notre Dame West, Montreal, Quebec H3C 1K3, Canada

[2] Finkl Steel-Sorel Inc., 100 McCarthy, Saint-Joseph-de-Sorel, Quebec J3R 3M8, Canada

compression tests are typically used to simulate the material response to thermomechanical processes, and then constitutive material models are developed to describe the stress–strain curves at different temperatures and strain rates [16, 17]. Different models have been developed to assess the individual and mutual influences of hot working process parameters on the flow stress evolution of stainless steel. Ying Han et al. [18] studied the hot deformation behavior of 904L superaustenitic stainless steels using the Arrhenius-type constitutive model. They reported that processing variables including strain, strain rate, and deformation temperature had a significant effect on the occurrence of DRX which was accelerated by increasing temperature and decreasing strain rate. Samantaray et al. [19] analyzed the high-temperature flow behavior of various grades of austenitic stainless steels, such as 304L, 304, 304 (as-cast), 316L, and alloy D9, using the modified Zerilli − Armstrong (MZA) model and found that the developed model predicted well the elevated temperature flow behavior over the entire ranges of strain rate, temperature, and strain. However, while a large number of efforts have been invested into the hot deformation behavior of austenitic stainless steels, little data is available on the martensitic grades.

In order to develop microstructure-based predictive tools for optimum thermomechanical processing, finite element simulation is used to predict strain, strain rate, and temperature all over the volume of the material as a function of processing conditions [20]. The implementation of a constitutive model would therefore allow correlating microstructure evolution to the local variations in strain, strain rate, and temperature. The constitutive models, which can predict the material flow behavior, are integrated into the FEM software. However, a very limited number of microstructure-based models have been integrated with the FEM software, and no report is available on the implementation of such models to study the hot workability of martensitic stainless steels.

Another predictive tool to determine the hot workability of a material based on changing the working parameters including temperature, strain, and strain rate is the processing maps proposed by Prasad et al. [21]. The maps are developed based on the dynamic material model (DMM), which provides processing conditions for a defect-free final product through optimizing the hot working parameters. The DMM technique provides the guidelines for avoiding the flow instability domains where inhomogeneous deformation and localized flow could take place. It also allows determining and locating the domains where a fine and homogenous microstructure develops during hot deformation. The different domains are obtained by the superimposition of a power dissipation map and an instability map for different temperatures, strains, and strain rates [22]. A large number of data have been reported on the application of the DMM method to various alloys, including stainless steels [23–25], but very few are on martensitic stainless steels [26, 27]. Furthermore, very little or no data is available on microstructure-based FEM modeling of hot deformation of stainless steels and its combination with processing map in general and martensitic ones, in particular [28].

In the present study, an accurate constitutive model for a modified AISI410 MSS which describes the flow stress in terms of hot working variables including strain, strain rate, and deformation temperature is developed. The derivation of actual stress from measured one caused by deformation heating and friction effect was corrected. A comparison is made between the experimental flow stress data and the one calculated by the established constitutive equations. The constitutive model that best predicts the flow curves was then implemented into the FEM code Forge NxT 3.0® software through the development of an original user subroutine (UMAT). The simulation results were first compared to the experimental ones for validation purposes and then were further utilized to analyze the effect of hot working parameters on microstructure evolution during the hot deformation process under different conditions. The DMM method was used to generate 3D processing maps which were correlated with the FEM and experimental results to discuss the hot deformation mechanisms and to determine the optimum hot working conditions.

2 Material and experimental procedures

The material used for the current investigation was supplied by Finkl Steel-Sorel Forge, Quebec, Canada. The production cycle starts with melting using a 45-ton electric arc furnace followed by ladle metallurgy degassing and refining processes along with tight control of the chemical composition. After the ingot-casting step, the solidified ingot is taken to the forge furnace and heated up to the forging temperature (1200–1260 ºC). The hot-forged ingot undergoes heat-treatment steps including the quench and tempering cycle. The samples for the isothermal compression test were cut from the ingot after hot forging. Figure 1 shows the position where the compression samples were cut from the large-size block and Table 1 displays the nominal chemical composition of the X12Cr13 used in this investigation.

The hot-compression tests were performed on cylindrical specimens with a diameter of 10 mm and a height of 15 mm based on the ASTM E209 standards with Gleeble 3800® thermomechanical simulator (Fig. 2a) at four different temperatures, 1050 ºC, 1100 ºC, 1150 ºC, and 1200 ºC and four strain rates, 0.001 s^{-1}, 0.01 s^{-1}, 0.1 s^{-1}, and 1 s^{-1}. The selected thermomechanical processing parameters are representative of the actual industrial forging process. The specimens were heated up to the test temperature at a heating
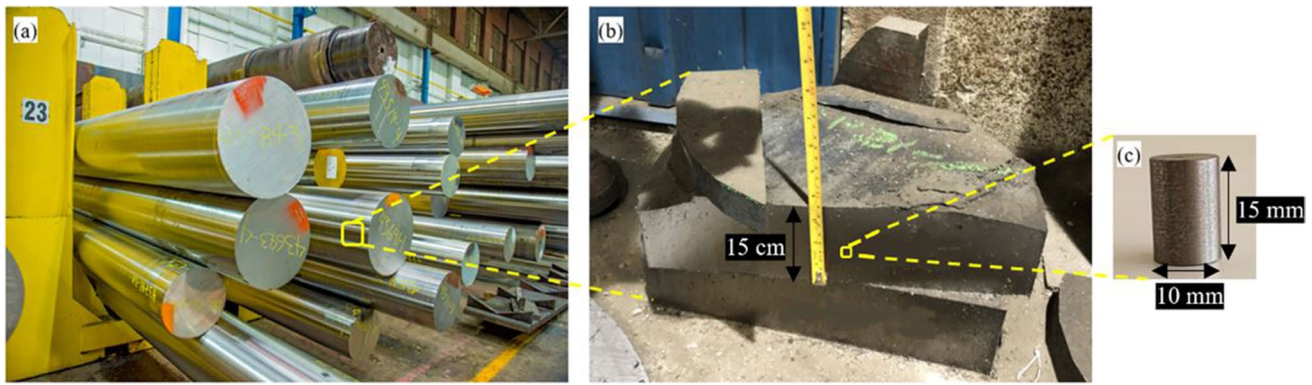
Fig. 1 An illustration depicting the position of the Gleeble test samples in the industrial-sized ingot

Table 1 The nominal chemical composition of the X12C13 (%wt.)

C	Mn	Cr	Si	P	Cu	Ni
0.14	1.03	11.71	0.25	0.19	0.15	0.48

Fig. 2 **a** Hot compression setup in the Gleeble machine; **b** three thermocouples placed at different locations of the sample for precise measurement of holding time; **c** sample before and after hot compression test
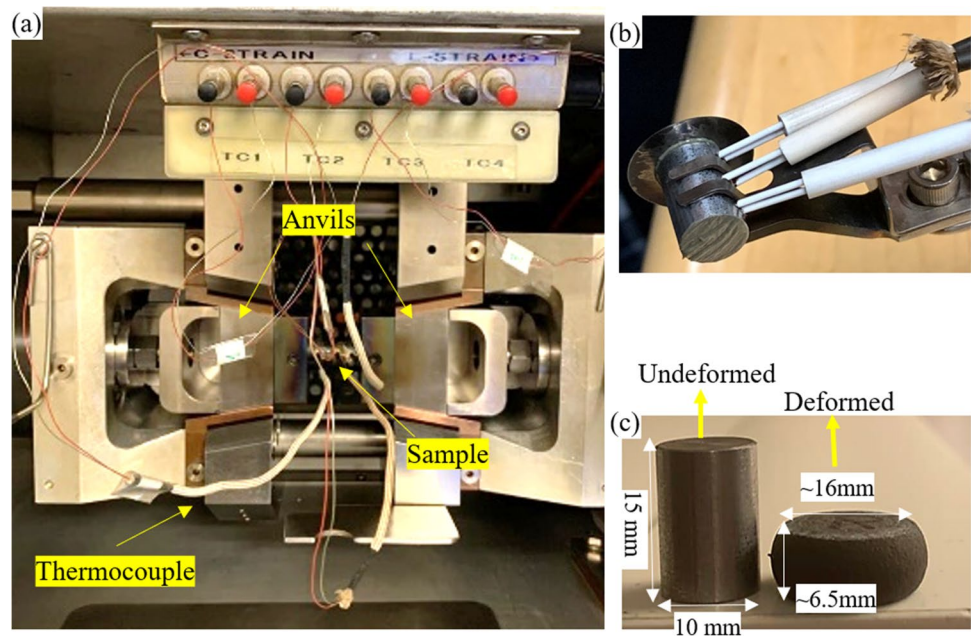
rate of 2 ºC/s, held for 15 min, and then subjected to compressive deformation at the selected strain rates. To ensure maximum uniformity and stability of temperature distribution over the entire sample and obtain a similar grain size, as the initial microstructure, three sets of thermocouples, one at the center and another two at the edges, as shown in Fig. 2b, were used to determine the optimum holding time of the target temperature. Figure 2c shows a sample before and after the hot compression test.

The temperature readings of all three thermocouples (TC) were recorded (Fig. 3a), and once the target temperature of 1230 ºC was reached, time was calculated until all three thermocouples gave the same reading. This confirmed the best time for uniform heat distribution in the specimen. On this basis, a 15-min holding time was determined for the temperature homogenization and used in all experiments. Figure 3b displays the schematic of the hot compression experiments, where it can be seen that after the 15-min holding time, the deformation is applied. Tantalum sheets of 0.1-mm thickness were used as a lubricant between the sample and the deformation anvils which are made of pure tungsten.

After cooling to room temperature, the deformed samples were cut parallel to the compression axis by a precision cutter machine for microscopic examinations. The specimens
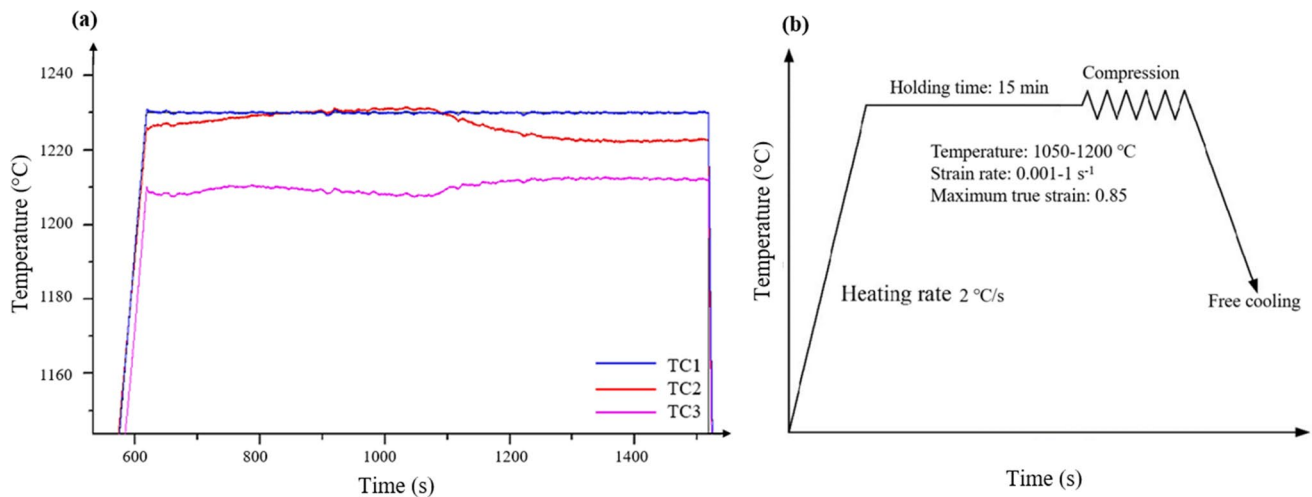
Fig. 3 **a** Influence of holding time at high temperature on temperature homogenization; **b** schematic illustration of a hot compression test

were mechanically polished down to 0.5 µm, and to reveal the microstructure, they were etched with Villela solution composed of 1 g $(O_2N)_3C_6H_2OH$, 5 ml HCL, and 100 ml C_2H_5OH for approximately 25 s. For microstructural characterizations, an Olympus LEXT OLS4100 laser confocal microscope was used.

3 Results and discussion

3.1 True stress–strain curves

The true stress–strain curves acquired from hot compression tests at different deformation temperatures and strain rates are shown in Fig. 4. It is seen that stress–strain curves are significantly affected by changing the temperature and strain rate. The flow curves decrease markedly with increasing temperature while for a fixed temperature, the flow stress increases with increasing the strain rate.

From the stress–strain curves of Fig. 4, three different stress changes can be observed with increasing stress. At the beginning of deformation (I), the stress increases significantly due to work hardening (WH). In the second stage (II), flow stress shows a continuous reduction with increasing stress until a peak point or an inflection of work-hardening rate. This shows that thermal softening, due to DRV and DRX, becomes more and more predominant until it exceeds WH. At the third stage (III), the stress curve shows three different patterns with the increasing strain: (i) gradual decrease to a steady state with DRV/DRX softening. This is the case for all deformation temperatures and strain rates between 0.001 and 0.1 s^{-1} except those at 1050 ℃ and 1100 ℃; (ii) higher stress levels without significant softening and work-hardening at 1050 ℃ and 1100 ℃ and strain rate of

0.1 s^{-1}; and (iii) continuous increase with significant work hardening (all deformation temperatures and strain rate of 1 s^{-1}) [24]. Therefore, it can be concluded that the softening due to DRX, characterized by a flow curve with a single peak followed by a steady-state flow, takes place at high temperatures and low strain rates. In contrast, at higher strain rates and lower temperatures, the higher work hardening rate slows down the rate of softening due to DRX, and therefore, both the peak stress and the onset of steady-state flow are shifted to higher strain levels. In fact, the drop observed in stress is because of dynamic recrystallization occurrence at all temperatures and strain rates of 0.001–0.1 s^{-1} in Fig. 4 [25]. Figure 5 shows the microstructure evolution at the end of deformation characterized by a significant grain refinement due to DRX (Fig. 5b) in comparison with the initial microstructure (Fig. 5a). However, at the strain rate of 1 s^{-1}, the flow curves are characterized by a continuous increase (without any peak), which is generally considered an indication of material undergoing DRV (Fig. 5c).

3.2 Corrections for deformation heating and friction effects

3.2.1 Deformation heating correction

During the hot compression test, part of the accumulated deformation energy can be transformed into heat resulting in a higher temperature than the nominal one [29]. This difference, directly, related to the applied strain rate [30] can cause some errors in measuring stress values by the equipment and needs to be corrected. At a low strain rate, the duration of deformation can provide enough time for the generated heat to dissipate into the surrounding environment, and therefore, the flow behavior is considered to be
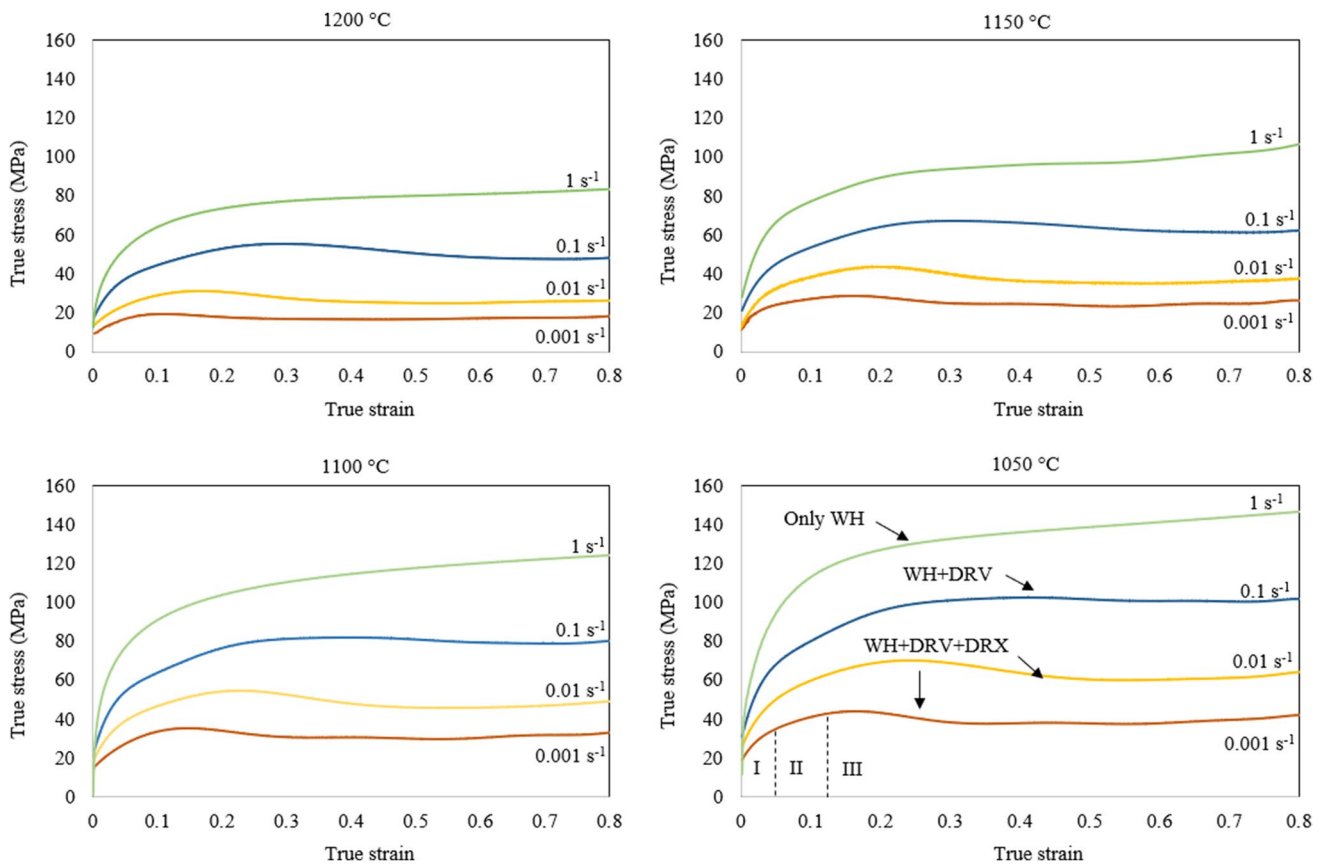
Fig. 4 True stress-true strain curves of the investigated steel at different deformation conditions
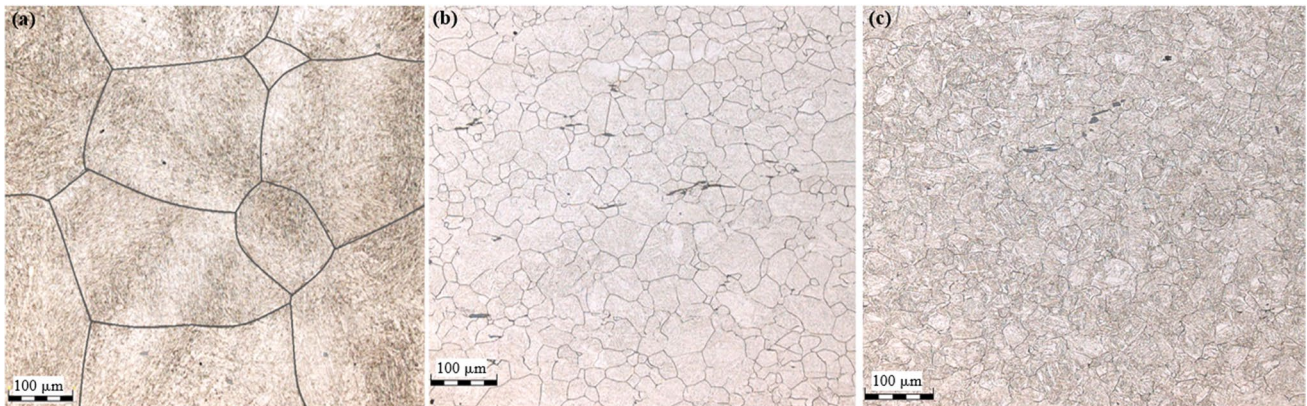

Fig. 5 Microstructure of the **a** as-received steel; **b** deformed sample at 1150 °C and 0.1 s^{-1}; **c** deformed sample at 1050 °C and 0.1 s^{-1}

under isothermal conditions. While at higher strain rates, the deformation heating cannot be fully removed from the sample, and consequently, the sample temperature rises. In this case, the process will be adiabatic. The following expression proposed by Goetz, R. Le is often used to correct the adiabatic heating effect [31]:

$$\Delta T = \frac{0.95\eta}{\rho C_p} \int_0^\varepsilon \sigma d\varepsilon \qquad (1)$$

where ρ is the material density, C_p is the specific heat, σ is the flow stress, ε is the strain, and η is the thermal efficiency being calculated as follows:

$$\eta = \begin{cases} 0 & \dot{\varepsilon} \leq 10^{-3} s^{-1} \\ 0.95 + (0.316) \log \dot{\varepsilon} & 10^{-3} s^{-1} \leq \dot{\varepsilon} \leq 1.0 \ s^{-1} \\ & \dot{\varepsilon} \geq 1.0 \ s^{-1} \\ 0.95 \end{cases}$$

(2)

The values of ρ and C_p in the case of the investigated steel were calculated using JmatPro simulation software (https://www.sentesoftware.co.uk/jmatpro) for different temperatures and are listed in Table 2.

The temperature increments were calculated using Eqs. (1) and (2) for strain values in the range of 0–0.8. Table 3 shows the variation of ΔT with $\dot{\varepsilon}$ for samples deformed at different strain rates and temperatures.

The results show a maximum temperature correction of about 16 ºC at the temperature of 1050 ºC and a strain rate of 1 s^{-1} that needs to be taken into consideration. The isothermal flow stresses (corrected for deformation heating), σ_c, were then determined using the following relationship [32]:

$$\sigma_c\left(\varepsilon, \dot{\varepsilon}, T_0\right) = \sigma_{wc}\left(\varepsilon, \dot{\varepsilon}, T_0\right) - \frac{\partial \sigma^H\left(T_0\right)}{\partial T_0}\bigg|\varepsilon\dot{\varepsilon}\Delta T$$

(3)

where σ_{wc} is the flow stress uncorrected for deformation heating and T_0 is the initial temperature. Figure 6 shows the correction of the adiabatic heating effect on true-strain curves of X12Cr13. The difference between corrected and uncorrected curves is increasing with increasing strain rate and decreasing temperature.

3.2.2 Friction correction

The presence of friction at the anvil-specimen interface leads to the formation of the dead zone and inhomogeneous deformation and therefore introduces errors in measuring

the flow stress during hot compression tests. Although tantalum sheets were used to lessen the friction, the impact of friction between anvil and specimen increases with increasing strain [33].

Figure 7a shows a schematic representation of the solid compression test where H_0 and R_0 are the initial height and radius of the cylinder, respectively. H is the height of the cylinder after deformation, and R_M and R_T are the maximum and top radius of the cylinder after deformation, respectively. To correct the flow stress, the friction coefficient μ was initially calculated using the equation "Friction coefficient" reported in Fig. 7b [28]. In this figure, b is the barreling factor, ΔR is the difference between the maximum and top radius ($\Delta R = R_M - R_T$), and ΔH is the difference between the initial and final height. After calculation of constants, the flow stress can be corrected by the equation "corrected stress" shown in Fig. 7b, where σ is the measured flow stress, σ_f is the corrected flow stress, and ε is the measured deformation degree. The corrected flow stresses for both adiabatic heating and friction effects are shown in Fig. 8. The experimental stress curves are higher than the corrected ones which suggest that the effect of friction was greater than adiabatic heating on flow stress. The corrected flow stress curves were then used in the establishment of the constitutive equation.

3.3 Constitutive modeling

3.3.1 Hansel-Spittel model

The Hansel-Spittel constitutive model [34] is currently implemented in Forge NxT 3.0® simulation software. This model relates flow stress to strain, strain rate, and temperature through the following equation:

$$\sigma = A e^{m_1 T} \varepsilon^{m_2} \dot{\varepsilon}^{m_3} e^{\frac{m_4}{\varepsilon}} (1 + \varepsilon)^{m_5 T} e^{m_7 \varepsilon} \dot{\varepsilon}^{m_8 T} T^{m_9}$$

(4)

Material constants, A and m_1 to m_9, can be derived from the stress–strain data obtained from hot compression tests [35]. In an initial stage, the above model was applied to the investigated steel, and the different material constants were calculated and are provided in Table 4:
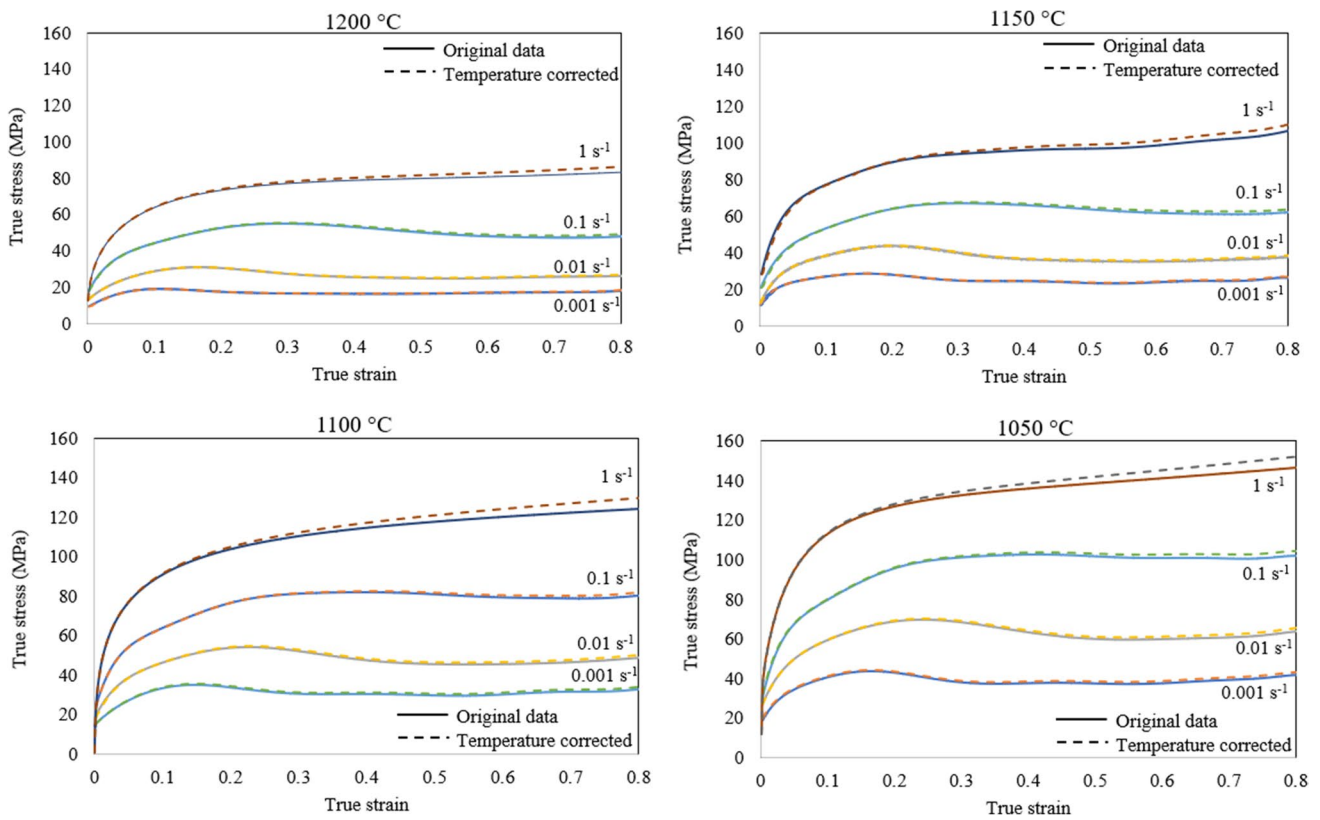
Table 2 Density and specific heat for different temperatures

Temperature (ºC)	1050	1100	1150	1200
Specific heat (J/g K)	0.64	0.65	0.66	0.67
Density (g/cm^3)	7.5	7.48	7.45	7.43

Table 3 Values of temperature increase during hot compression tests

	0.001 s^{-1}		0.01 s^{-1}		0.1 s^{-1}		1 s^{-1}	
	T (ºC)	ΔT	T (ºC)	ΔT	T (ºC)	ΔT	T (ºC)	ΔT
	1050	2.91	1050	4.74	1050	7.64	1050	15.90
	1100	2.38	1100	3.675	1100	6.12	1100	13.48
	1150	1.81	1150	2.85	1150	4.97	1150	11.05
	1200	1.23	1200	1.95	1200	3.84	1200	8.87

Fig. 6 Flow stress curves corrected for the effect of adiabatic heating

Fig. 7 a Simple representation of the sample's geometry before and after the compression test; **b** friction corrected formulas [33]
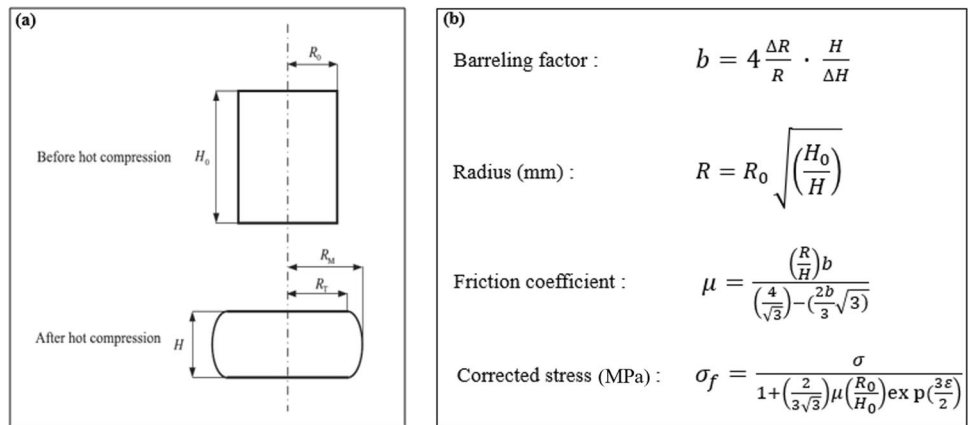

Figure 9 shows the comparison between the experiment and calculated flow stress based on the Hansel-Spittel model. It can be seen that the difference between experimental and predicted stress is significant, especially at higher strain rates. The results also show that this model is not able to predict the softening behavior of the studied alloy for any of the investigated deformation conditions. Therefore, another constitutive model is needed to more accurately predict the flow stress behavior of the investigated steel.

3.3.2 Arrhenius equation

The Arrhenius-type equation initially proposed by Sellars and McTegart relates the strain rate, temperature, and the activation energy at a constant strain value, through the following equation [36]:

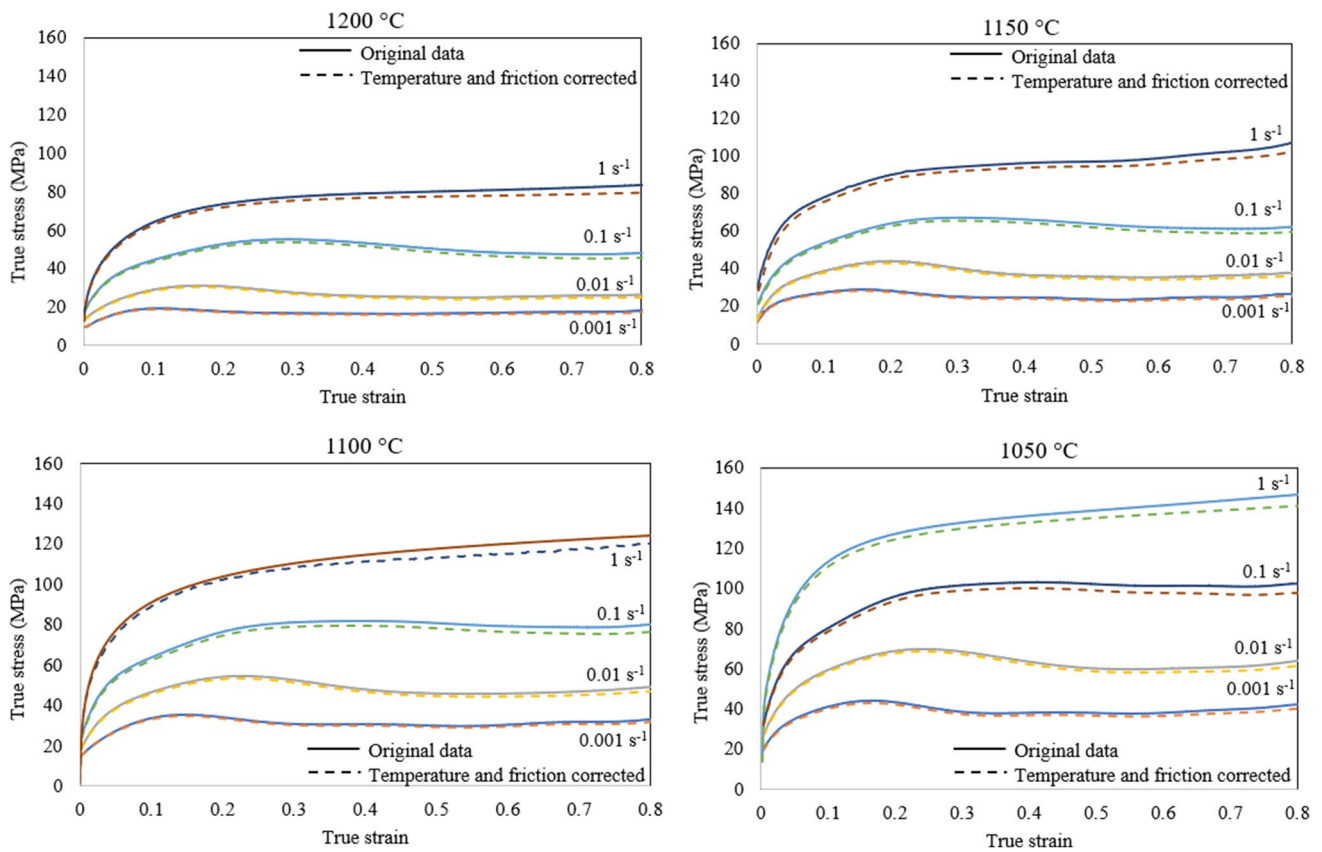$$Z = \dot{\varepsilon} exp\left(\frac{Q}{RT}\right) = A[sinh(\alpha\sigma)]^n \tag{5}$$

Fig. 8 Corrected flow stress curves due to the friction and adiabatic heating effects for tested temperatures and strain rates

where Z is the Zener-Hollomon parameter, Q is the activation energy required to overcome deformation barriers, A, α (MPa^{-1}), and n are material constants, R the universal gas constant, T the temperature in Kelvin, $\dot{\varepsilon}$ is the strain rate, and σ is the applied stress.

According to Eq. (5), the flow stress of the material, at a given strain, can be expressed as follows:

$$\sigma = \frac{1}{\alpha}[\sinh^{-1}(\frac{Z}{A})]^{\frac{1}{n}} \tag{6}$$

After some algebraic operations, the following expression is used to calculate the predicted stress:

$$\sigma = \frac{1}{\alpha}ln\left\{(\frac{Z}{A})^{\frac{1}{n}} + \sqrt{(\frac{Z}{A})^{\frac{2}{n}} + 1}\right\} \tag{7}$$

The Arrhenius equation has the advantage to be physics-based by including the activation energy term and therefore

is more sensitive to changes in the microstructure. The strain rate during high-temperature deformation is given by [37, 38]:

$$\dot{\varepsilon} = AF(\sigma)exp(-\frac{Q}{RT}) \tag{8}$$

where $F(\sigma)$ is in the form of power function:

$$F(\sigma) = \begin{cases} \sigma^{n1} & \alpha\sigma < 0.8 \\ exp(\beta\sigma) & \alpha\sigma > 1.2 \\ [sinh(\alpha\sigma)]^n & (\text{for all } \sigma) \end{cases} \tag{9}$$

The constants n_1 and β are the slopes of the curves $ln\dot{\varepsilon}$ vs. $ln\sigma$ and $ln\dot{\varepsilon}$ vs. σ, respectively, as indicated in Eq. (10) and illustrated in Fig. 10.

$$n_1 = \frac{\partial ln\dot{\varepsilon}}{\partial ln\sigma}, \beta = \frac{\partial ln\dot{\varepsilon}}{\partial\sigma} \tag{10}$$

Thus:

Table 4 Parameters of Hansel-Spittel equation

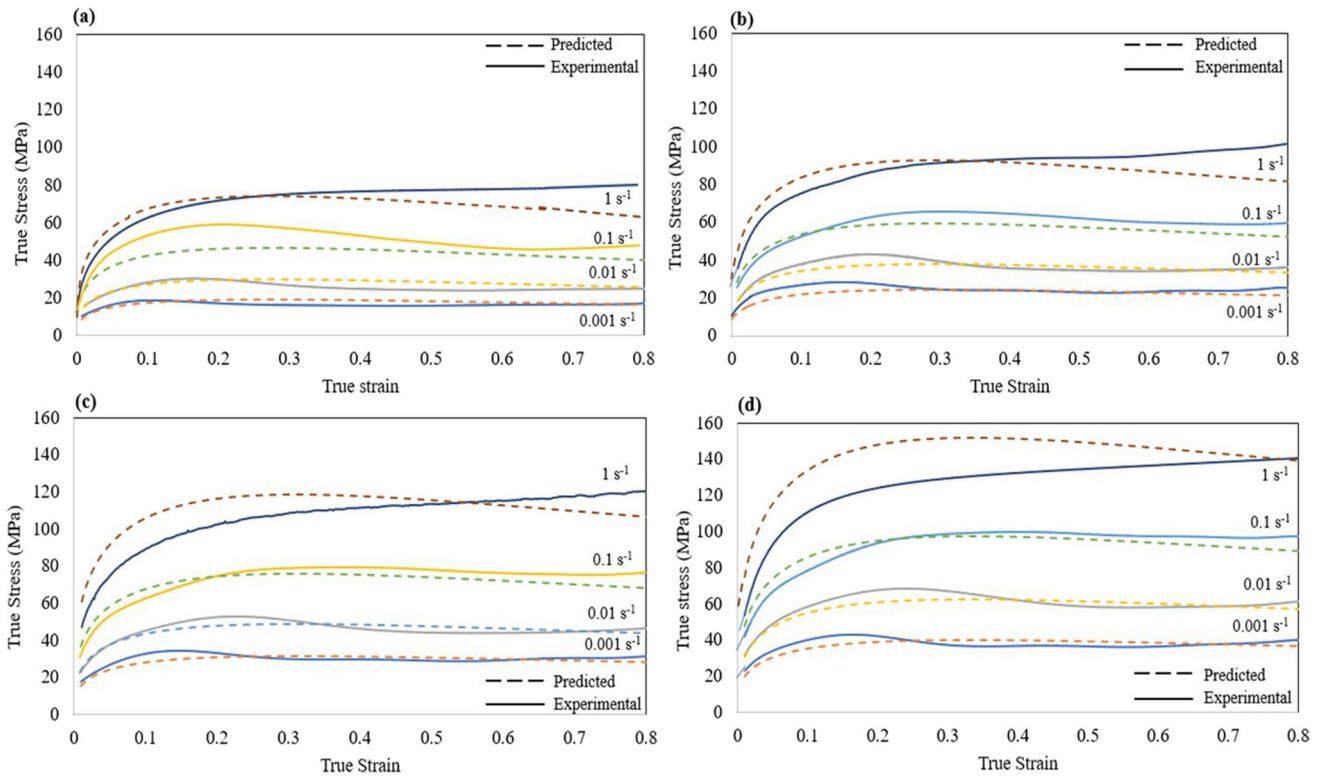| A	m_1	m_2	m_3	m_4	m_5	m_7	m_8	m_9
−135.39	−0.024	0.297	−0.103	−0.0002	−0.0013	0.139	0.00026	24.02

Fig. 9 Comparison between the experimental and calculated flow stress developed by Hansel-Spittel model at four strain rates and temperatures of **a** 1200 ℃, **b** 1150 ℃, **c** 1100 ℃, **d** 1050 ℃

$$\alpha = \frac{\beta}{n_1} \tag{11}$$

Similarly, the constant n is the slope of the curve $ln\dot{\varepsilon}$ vs. $ln[sinh(\alpha\sigma)]$ as indicated in Eq. (12) and reported in Fig. 10d [39]:

$$n = \frac{\partial ln\dot{\varepsilon}}{\partial ln[sinh(\alpha\sigma)]} \tag{12}$$

For determining constant A, the activation energy, Q, should be calculated first. For a specific strain rate, the slope of $ln[sinh(\alpha\sigma)]$ vs. T^{-1} gives the values of $\frac{Q}{nR}$ by linear regression of each curve. Thus, Q is obtained by substituting $R = 8.314$ J.mol^{-1} K^{-1} and calculating n:

$$Q = Rn\frac{\partial ln[sinh(\alpha\sigma)]}{\partial(\frac{1}{T})} \tag{13}$$

Finally, "A" is the intercept of the curve lnZ vs. $ln[sinh(\alpha\sigma)]$. The constant values are listed in Table 5, and the plots used to obtain all constants are shown in Fig. 10.

As indicated above, the Arrhenius equation is based on constant strain condition. Moreover, as shown in Fig. 8,

the impact of strain on the flow stress is significant; thus, it is necessary to take the strain term into account for a more accurate constitutive equation. The evolution of the above material constants with strain could be described through polynomial functions of strain, as also reported in the literature [40–42]. As illustrated in Fig. 11, in the present study, it is possible to obtain an accurate fitting of the different constants with the applied strain using a sixth-order polynomial.

The sixth-order polynomial fit results are obtained as given in Eq. (14):

$$n = 4.776 + 11.181\varepsilon - 140.46\varepsilon^2 + 517.92\varepsilon^3 - 901.73\varepsilon^4 + 766.97\varepsilon^5 - 256.54\varepsilon^6$$

$$\alpha = 0.0307 - 0.2058\varepsilon + 1.2646\varepsilon^2 - 3.8842\varepsilon^3 + 6.3855\varepsilon^4 - 5.3762\varepsilon^5 + 1.8174\varepsilon^6$$

$$Q = 485.31 + 29.685\varepsilon - 1353.9\varepsilon^2 - 4448.6\varepsilon^3 + 29723\varepsilon^4 - 45492\varepsilon^5 + 22050\varepsilon^6 \tag{14}$$

$$lnA = 37.311 + 11.868\varepsilon - 213.31\varepsilon^2 + 30.281\varepsilon^3 + 1724.8\varepsilon^4 - 3112\varepsilon^5 + 1598.6\varepsilon^6$$

After developing the models of n, α, Q, and lnA by considering the effect of strain, the flow stress can be predicted using Eq. (7) which relates the stress to the Zener-Hollomon parameter, strain rate, deformation temperature, and the material constants as a function of strain [43].
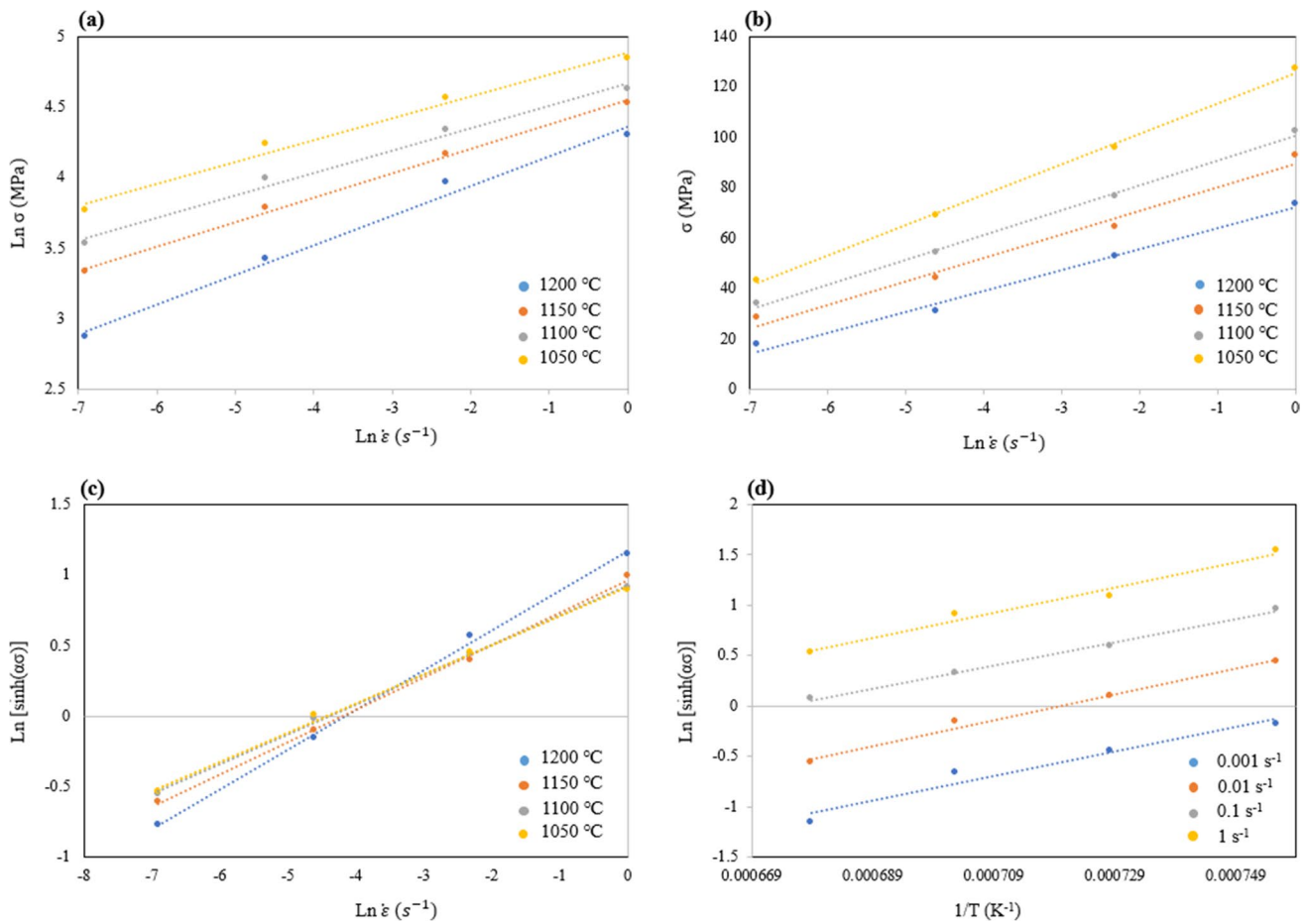
Fig. 10 Plots for determination of the constants **a** n_1, **b** β, **c** n, **d** Q at a deformation temperature of 1200 °C, 1150 °C, 1100 °C, and 1050 °C. The constants represent the slope of the respective curves determined using linear regression

3.4 Verification of the developed constitutive equations

To evaluate the accuracy of the developed constitutive models in predicting the hot deformation behavior of the martensitic stainless steel, the predicted value should be compared with the experimental one. As shown in Fig. 12, a good agreement can be observed between the experimental data and the predicted values for all of the experimental conditions used in this work.

The accuracy and the reliability of the Arrhenius model were compared in terms of correlation coefficient (R) and the average absolute relative error (ARRE Δ):

$$R = \frac{\sum_{i=1}^{N}(\sigma_E^i - \overline{\sigma}_E)(\sigma_P^i - \overline{\sigma}_P)}{\sqrt{\sum_{i=1}^{N}(\sigma_E^i - \overline{\sigma}_E)^2 \sum_{i=1}^{N}(\sigma_P^i - \overline{\sigma}_P)^2}} \tag{15}$$

The absolute average error (Δ) is expressed as:

$$\Delta = \frac{1}{N}\sum_{i=1}^{N}\left|\frac{\sigma_E^i - \sigma_P^i}{\sigma_E^i}\right| \times 100 \tag{16}$$

where σ_E is the experimental data, and σ_P is the calculated value based on the proposed constitutive equations. $\overline{\sigma}_P$ and $\overline{\sigma}_E$ are the mean values of σ_P and σ_E, respectively, and N is the number of data points. The calculated R coefficient is shown in Fig. 13b, where a good correlation can be observed between the measured and calculated data.

It must be noted that the value of the R coefficient indicates the intensity of a linear relationship between the predicted and the experimental values. However, a higher R-value is not always indicative of the higher accuracy of the model because the model is often biased towards higher or lower values. Therefore, an unbiased statistical parameter,

Table 5 Material constants in the Arrhenius model

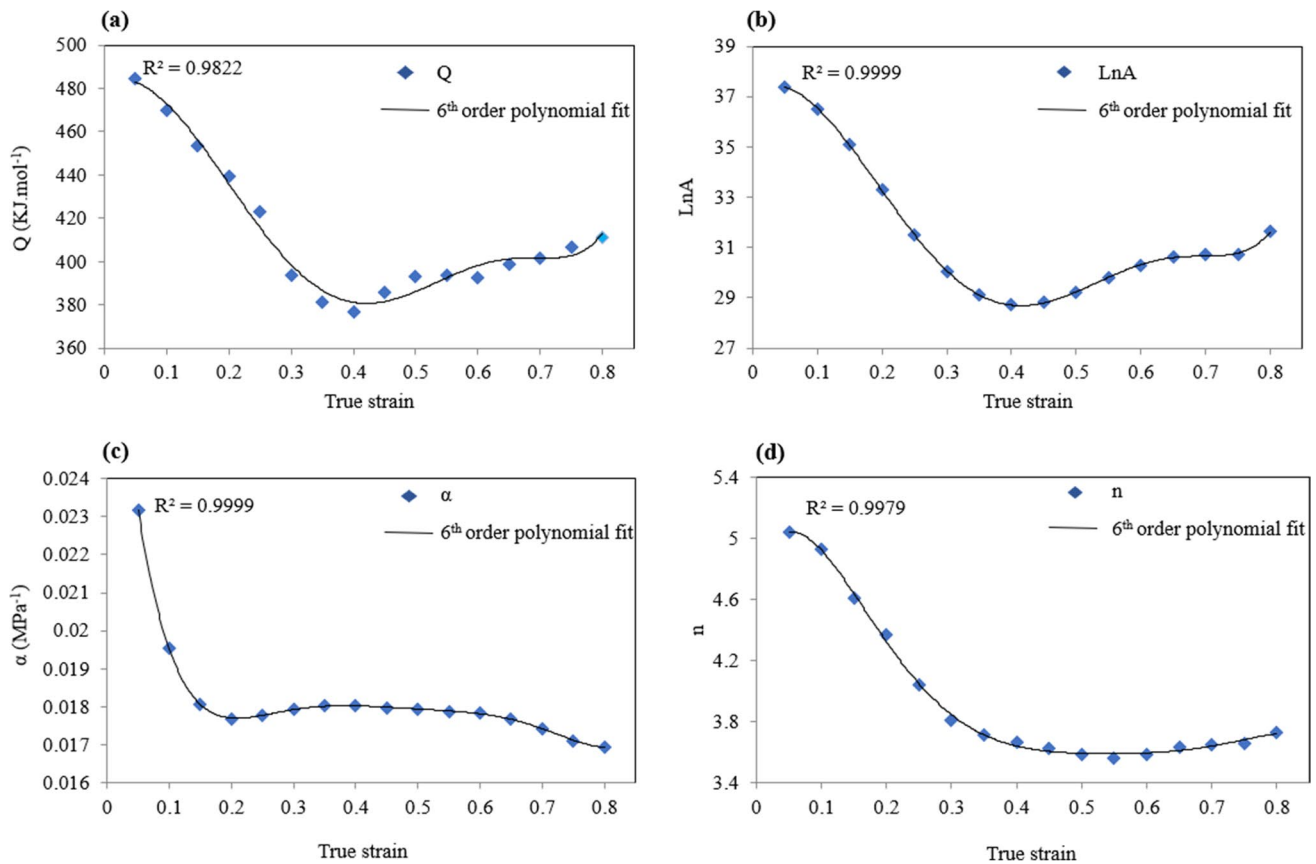| β (MPa^{-1})	n_1	α (MPa^{-1})	n	Q (KJ mol^{-1})	LnA
0.097021	5.3010	0.0181	3.95	412.948	31.463

Fig. 11 The polynomial fit of order 6 of variation of; **a** *Q*, **b** *lnA*, **c** *α*, **d** *n*. The blue square denotes experimental data and the black line denotes polynomial models

Δ, is used to evaluate the accuracy of the Arrhenius model in prediction [4]. The lower is the absolute average error, the higher is the predictability of the model. The values of Δ at different temperatures and strain rates are listed in Fig. 13b. It can be seen that the maximum value is 5.04% at the strain rate of 0.01 s^{-1} and the deformation temperature of 1200 ℃. The minimum value is 0.81% at the strain rate of 0.1 s^{-1} and the deformation temperature of 1050 ℃, and the mean value of Δ for all the deformation conditions is 3.29% which is a very small error. Thus, it could be concluded that the established constitutive equations can well describe the relationship between flow stress, strain rate, temperature, and strain. However, the developed constitutive equation should be implemented in Forge NxT 3.0® software in order to predict temperature, strain, and strain rate maps in different locations of the specimen and then validate the predictions through microstructure examination.

3.5 Microstructure-based FEM simulation

A specific user subroutine was developed to implement the constitutive equation in the FE code. For the analysis, three-dimensional finite element method was performed to simulate

the hot compression process. The boundary conditions for the FE simulations were similar to the experimental tests (i.e., temperature, strain rate, strain, and thermal exchange between piece and anvils). The friction factor was selected as 0.35, and the convergence tests were performed by changing the element size to ensure the accuracy. The numerical simulations were performed on a FEM model discretized with four-node tetrahedral elements. Figure 14a and b show the meshed finite element models before and after deformation respectively, and Fig. 14c shows a comparison between the predicted and experimental data of force versus time where good and acceptable predictability of the model is demonstrated.

According to simulation results, the strain distribution can be illustrated as a contour plot aided by color series at the temperature of 1050–1200 ℃, shown in Fig. 15a–d. In this figure, the non-uniformity of deformation distribution is seen. The specimen is roughly divided into several deformation zones (non-uniformity) according to the severity of deformation, which leads to different flows of material during hot deformation and different microstructure evolution. Figure 16 shows the microstructure evolution during an upset operation at 1200 ℃ and a strain rate of 0.1 s^{-1}. The specimen was cut parallel to
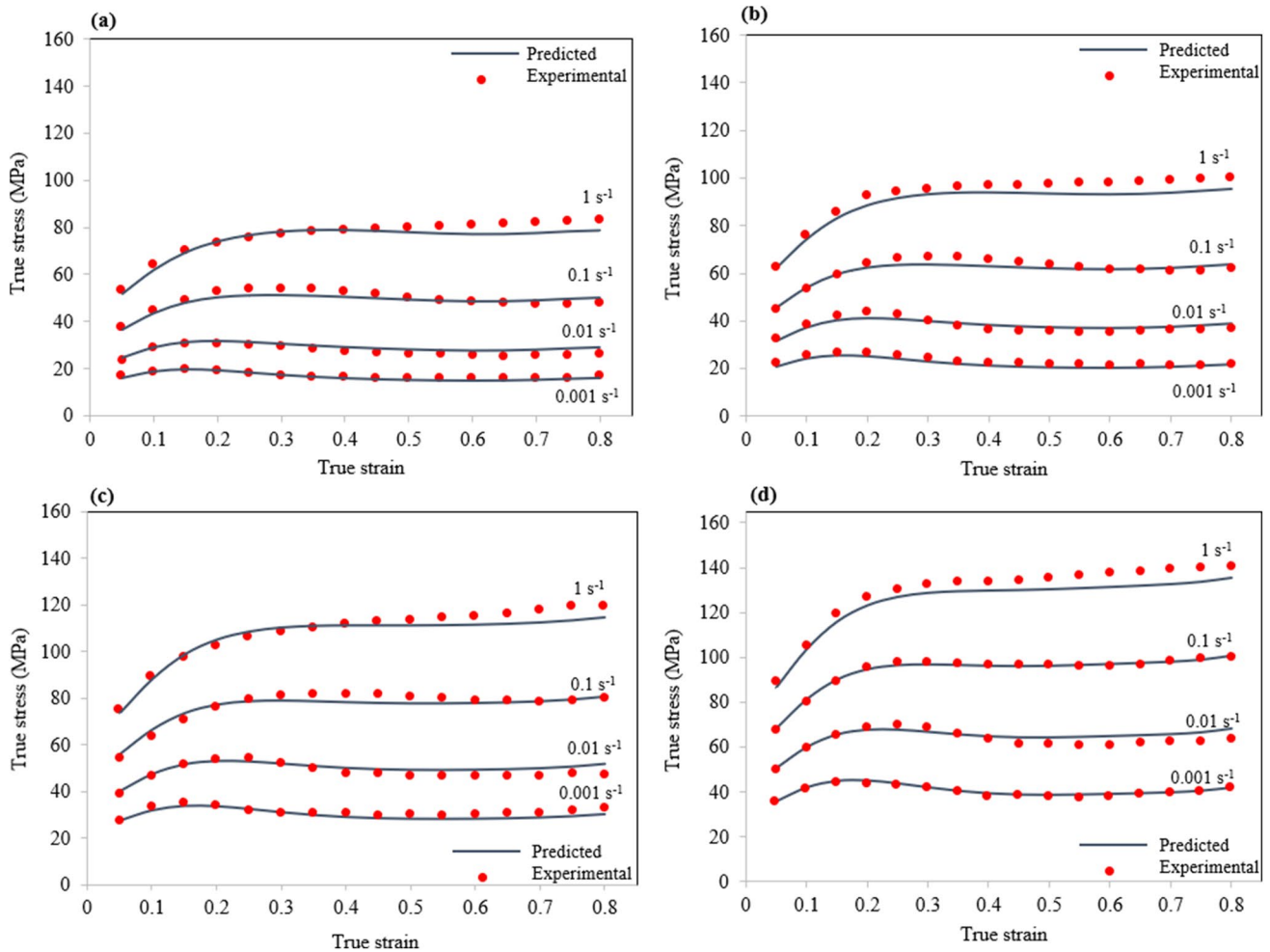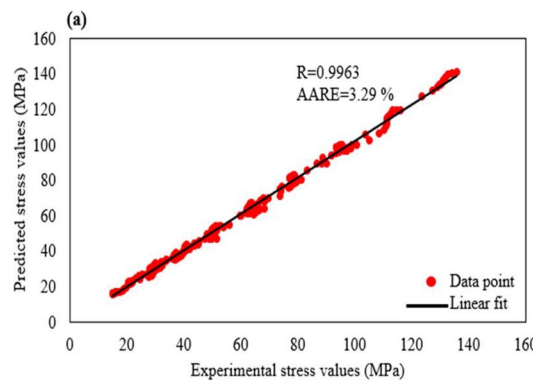
Fig. 12 Comparison between the experimental and calculated flow stress developed by Arrhenius model at 4 strain rates and temperatures of **a** 1200 °C, **b** 1150 °C, **c** 1100 °C, **d** 1050 °C

Fig. 13 **a** Correlation between the experimental and calculated flow stresses by the developed constitutive equation; **b** value of Δ at different temperatures and strain rates

$\dot{\varepsilon}\ (s^{-1})$	Δ (%)			
	1200 °C	1150 °C	1100 °C	1050 °C
0.001	3.06	4.6	4.54	2.03
0.01	5.04	4.2	4.13	3.73
0.1	3.15	1.36	2.32	0.81
1	2.68	3.36	1.37	3.25

the compression axis by a precision cutter machine for carrying out a metallographic examination. The circled numbers in Fig. 16a, represent strain levels that the material experienced during hot deformation, based on the map of strain distribution, and the yellow dotted lines show the

dead zones. In Fig. 16b–e, the microstructure of the corresponding four zones is shown.

As shown in Fig. 16b, for material regions that experienced a strain of 0.2, the microstructure remained unchanged due to a low degree of deformation. By increasing strain, Fig. 16c,
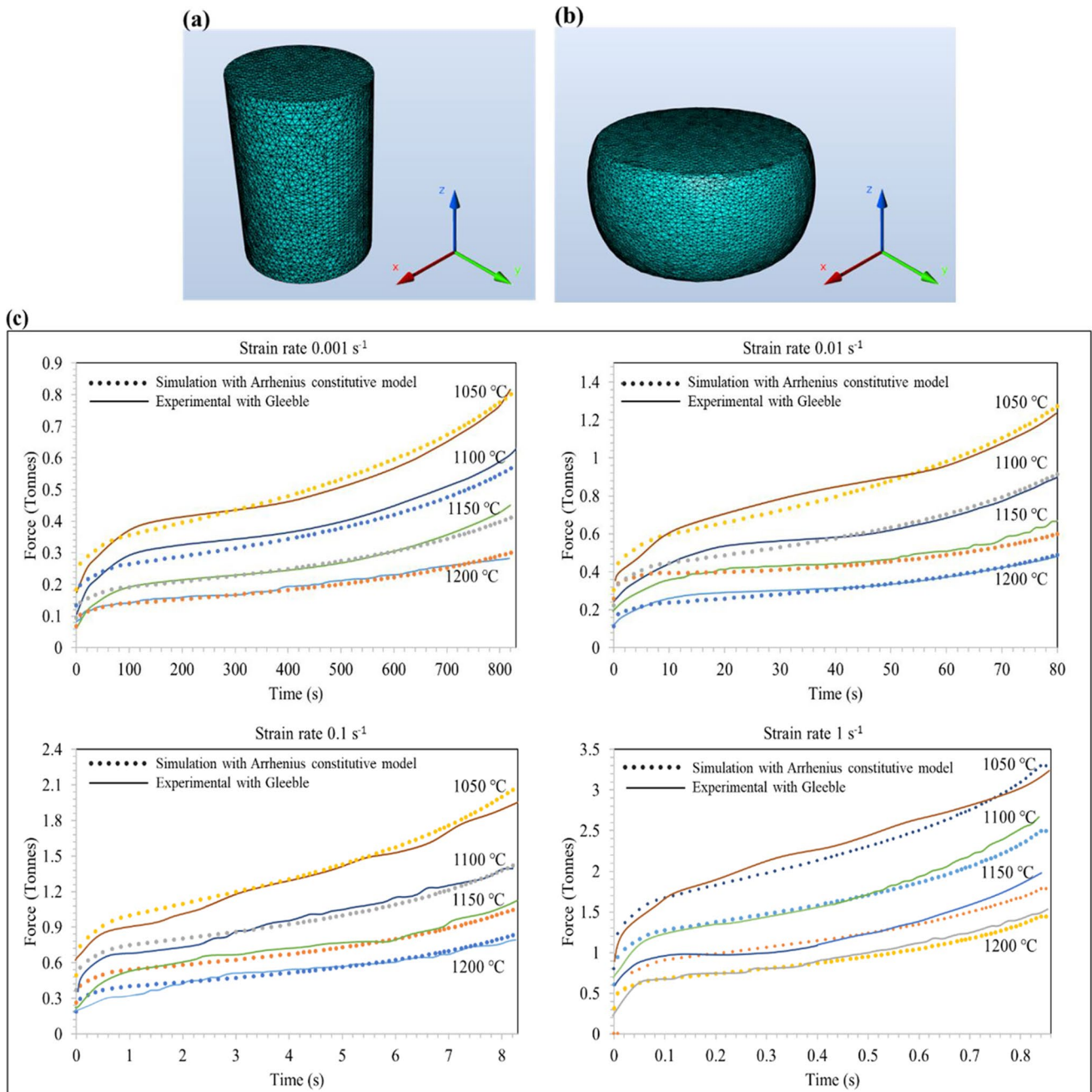
Fig. 14 FE model **a** before deformation; **b** FE model after deformation; **c** force versus time plot of experimental and predicted for all deformation conditions

the nucleation of new grains around the initial grain boundaries can be seen indicating that the workability of the material increased through recrystallization. The microstructure at strain of 0.4 is heterogeneous with a mix of deformed and undeformed grains which makes the material susceptible to the occurrence of defects and wedge cracking, thereby deteriorating the mechanical properties. However, the material is fully

recrystallized at the strain of 0.6 and 0.8, as shown in Fig. 16d and e, respectively.

3.6 Processing map

The part with fewer defects in the final production process signifies the ideal processing conditions and higher
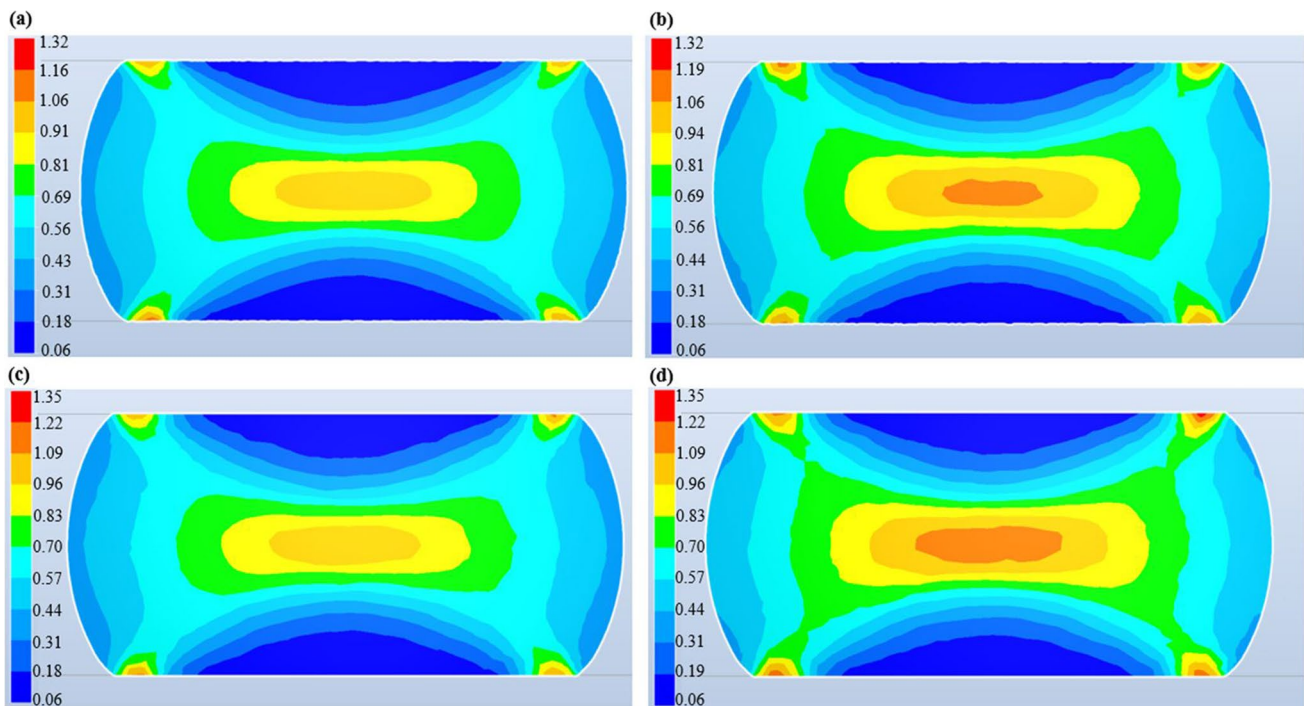
Fig. 15 FE results of effective strain distribution in the sample deformed to a strain of 0.8 and a strain rate of 0.1 s^{-1} **a** 1200 ℃, **b** 1150 ℃, **c** 1100 ℃, and **d** 1050 ℃

workability of metal, which means the higher plastic deformation ability that a metal can be deformed easily without fracture during the forming process. In 1997, Prasad and colleagues proposed the deformation mechanism model (DMM) which produces the flow instability domains [21]. This model is an analytical method used to determine optimum deformation temperature and strain rate ranges in hot forming operations. Based on the DMM, the workpiece undergoing hot deformation goes through a process of power dissipation (P), defined by Eq. (17). The total input power is dissipated through plastic work that is converted into heat (G) and changes in the microstructure (J), such as flow localization, DRV, DRX, phase transition, and shear band formation [44].

$$P = G + J = \int_0^{\dot{\varepsilon}} \sigma d\dot{\varepsilon} + \int_0^{\sigma} \dot{\varepsilon} d\sigma = \sigma \dot{\varepsilon} \tag{17}$$

The flow stress, at constant strain and deformation temperature, is given by [45]:

$$\sigma = K \dot{\varepsilon}^m \tag{18}$$

where K is a material constant, and m is the strain rate sensitivity and can be represented as follows:

$$m = \frac{\partial(ln\sigma)}{\partial(ln\dot{\varepsilon})} \tag{19}$$

By comparison of J co-content with the maximum possible dissipation, the dimensionless parameter, η, efficiency of power dissipation is defined as

$$\eta = \frac{J}{J_{\max}} = \frac{2m}{m+1} \tag{20}$$

η represents the ability of the workpiece to change its microstructure upon deformation. By plotting contours of η as a function of temperature and strain rate, a power dissipation map is obtained.

Softening mechanisms such as DRX and DRV are associated with η. However, in the case of void formation or wedge cracking, the power dissipation map alone is not sufficient to fully characterize the hot working behavior of an alloy. In order to achieve this and, in particular, to optimize the processing parameters, it is important to distinguish the undesirable regions characterized by the unstable flow. The instability criteria are defined in order to identify such regions and

Fig. 16 Optical microscope views of **a** deformed sample at 1200 ℃ and a strain rate of 0.1 s^{-1} to strains of **b** 0.2, **c** 0.4, **d** 0.6, and **e** 0.8
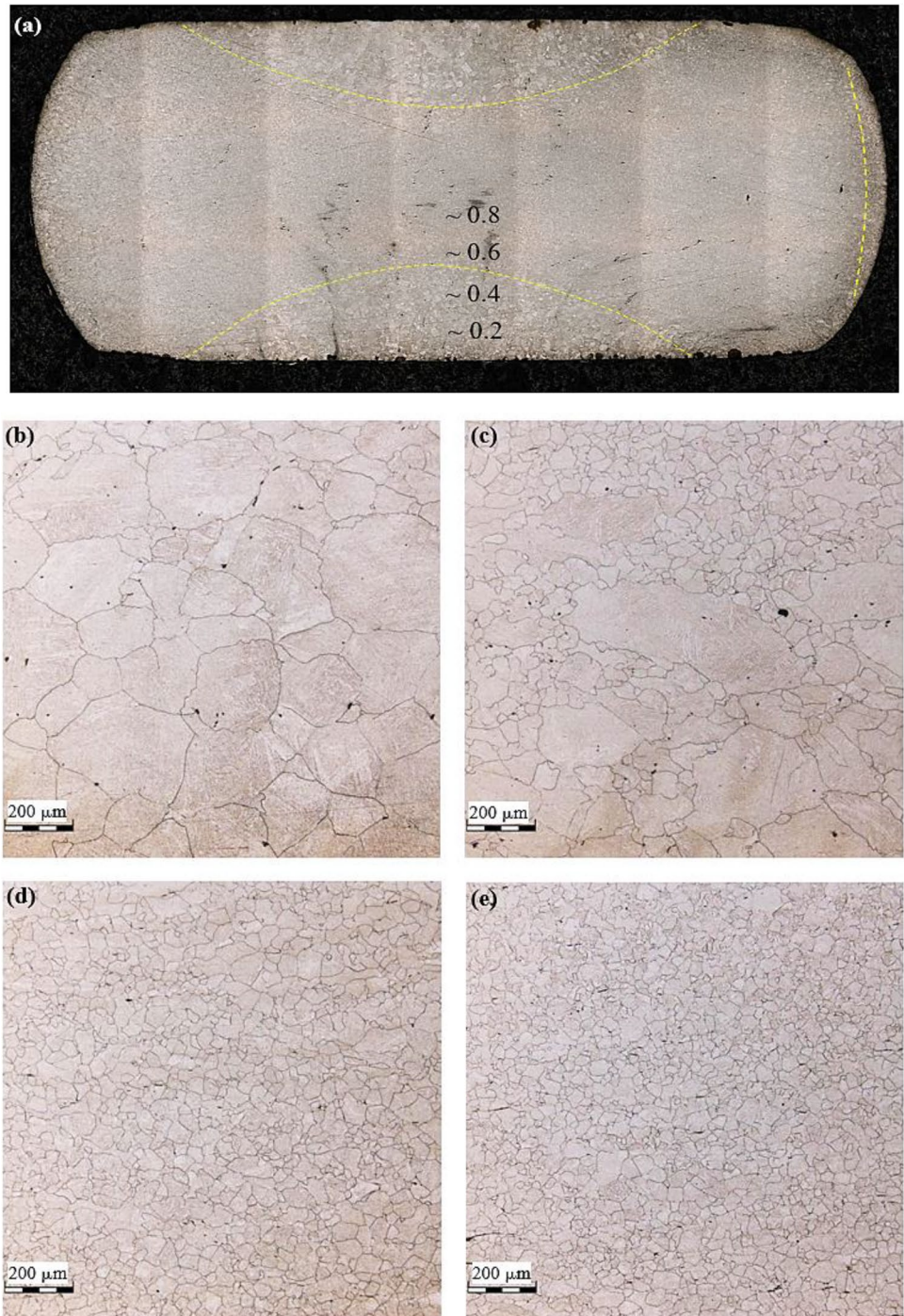

build an instability map that, once superimposed on the iso efficiency contours, provides the final processing map.

Instability maps are developed based on Ziegler's plasticity theory to the dissipation functions of the dynamic materials model. A dimensionless parameter for microstructural instability based on Kumar-Prasad and Murty-Rao criteria, [46], respectively, is given by

$$\xi(\dot{\varepsilon}) = \frac{\partial \ln(\frac{m}{m+1})}{\partial \ln \dot{\varepsilon}} + m < 0 \tag{21}$$

As reported by Ziegler et al. [47], mixed microstructure, flow localization, or adiabatic shear bands are susceptible to occur in regions with negative ξ values.

Fig. 17 The 2D processing map at various strains **a** 0.2, **b** 0.4, **c** 0.6, **d** 0.8
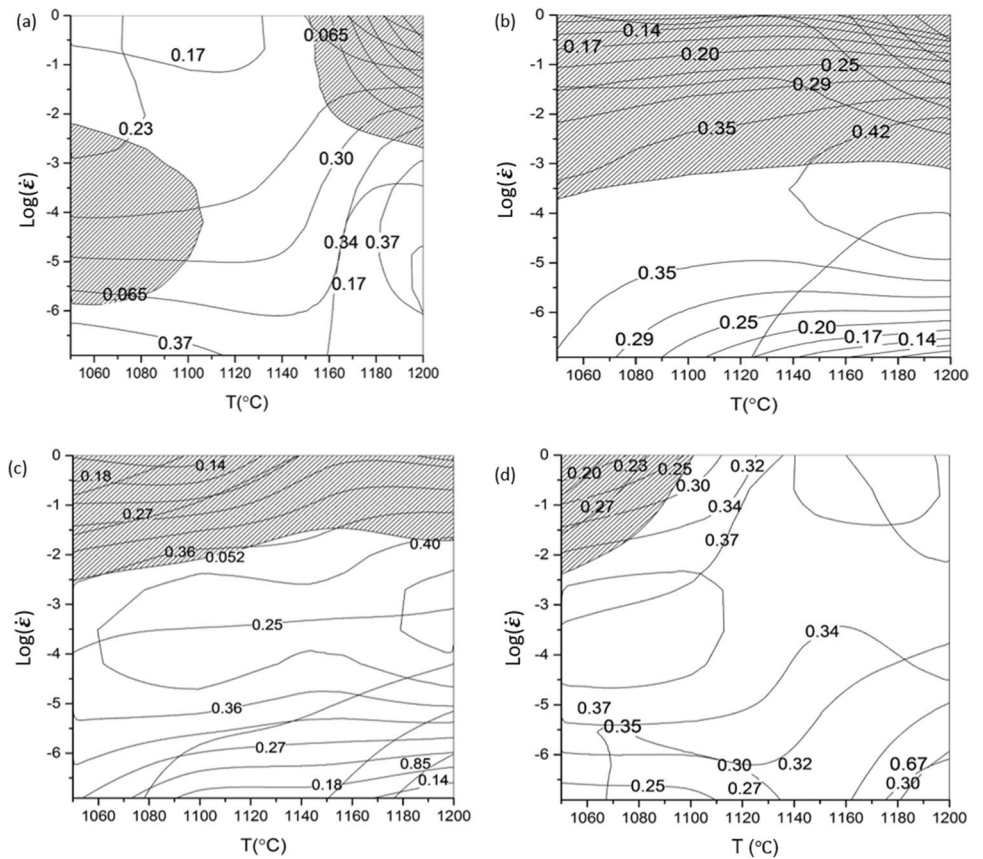
3.6.1 The 2D processing maps at various strains

2D processing maps can be obtained through the superimposition of the power dissipation and flow instability 2D contour maps at a given strain. Figure 17 shows the 2D processing maps of the X12Cr13 investigated steel at various

strains with an interval of 0.2. It can be seen from the figure that, by increasing the strain, the maximum power efficiency increases while the flow instability region first increases up to 0.4 strain and then decreases. Moreover, the flow instability occurred for the highest strain rate ($\dot{\varepsilon} = 0.182$ s^{-1} – 1 s^{-1}). The occurrence of such flow instability could be related to the
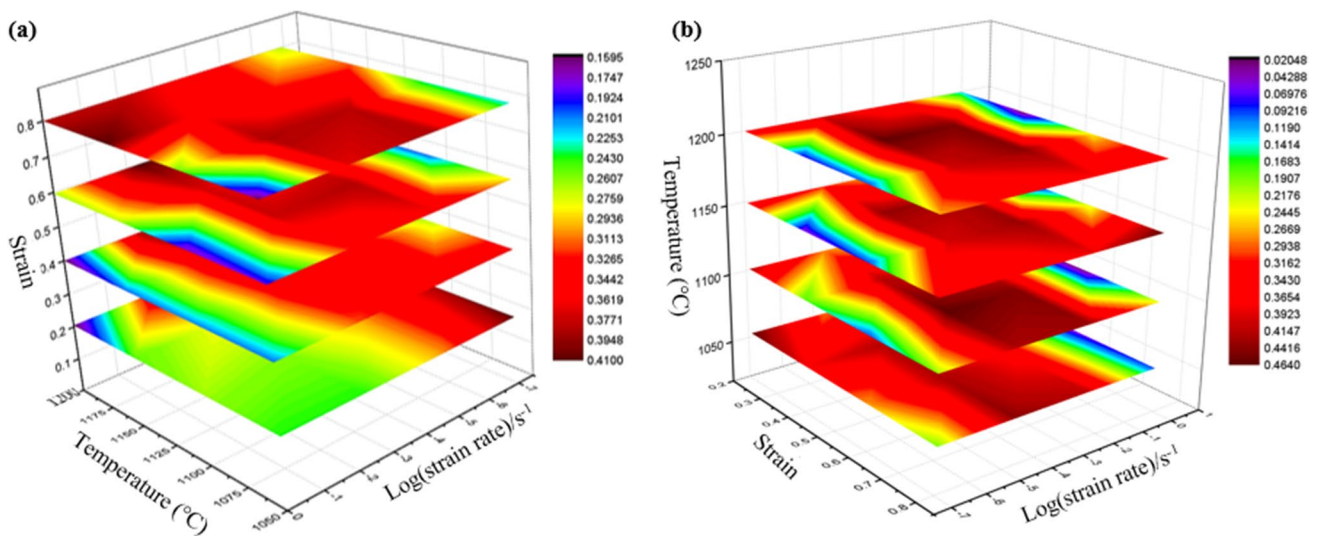

Fig. 18 The 3D power efficiency map as a function of **a** strain and **b** temperature

limited time for dislocation movement due to the high strain rate and the subsequent inhibition of softening processes such as DRV and DRX. Under these conditions, strain accumulation could be restricted to specific regions and the formation of wedge crack, voids, and shear bands is promoted, as also reported by Momeni et al. [22]. Therefore, hot working parameters should be selected carefully to avoid regions with a negative value for the flow instability parameter which corresponds to the gray-shaded regions in Fig. 17.

3.6.2 Continuous 3D processing maps

In the power dissipation maps of Fig. 17, the color of the grid is related to the value of the power dissipation efficiency parameter η. As shown in Fig. 18, η value increases by increasing strain and temperature. This means that higher η leads to higher workability and increased potential for microstructural changes. Based on the above findings, because significant microstructural evolution via DRX occurs in the region with the highest η-value, the deformation should be carried out in this region.

The processing map has been used to identify unstable and risky situations through the determination of two factors: power dissipation and flow instability domains. The results obtained in the present investigation show a good agreement between the DMM results and those obtained with FEM simulation and microstructure observations. These results are interesting as it is the first time such comparison is made between the predictions of the two methods and supported by experimental evidence. Specifically, the non-uniformity of strain distribution during the deformation, predicted by the FEM analysis, was confirmed by microstructure examination, as reported in Fig. 16. The processing map analysis shows that regions that experienced a lower strain have negative instability values and low power efficiency which means that they have low workability. In Fig. 16c, the microstructure at strain of 0.4 is heterogeneous and is expected to have inconsistent mechanical properties. This finding agrees with the negative instability criteria reported in Fig. 17b. On the other hand, as reported in Fig. 16d and e, the material is fully recrystallized at the strains of 0.6 and 0.8, respectively. The DMM analysis also showed that under these conditions, the instability criteria have a positive value (not gray-shaded regions) which means higher workability as shown in Fig. 17c and d.

4 Conclusion

The hot workability of a martensitic stainless steel was studied using microstructure-based numerical simulation. The following conclusions can be drawn from the present investigation:

1. The flow stress curves of the compressed X12Cr13 steels in the range of 1050–1200 °C and the strain rate range of 0.001–1 s^{-1} display a significant sensitivity of flow stress to strain rate, temperature, and strain.
2. A constitutive equation based on the Arrhenius model was developed in the present work and its validity was confirmed showing more accurate prediction than the Hansel-Spittel model.
3. The developed constitutive model was integrated into the Forge NxT 3.0® software and showed good correlations with the predictions of flow instability domains obtained using the dynamic material model.

Author contribution Simin Dourandish: conducting the experimental tests and numerical analysis, methodology, writing, reviewing, and editing the paper

Henri Champliaud: finite element modeling, reviewing, and editing

Mohammad Jahazi: idea of the project, definition of the project, review of the methodology and experimental part, supervision, reviewing, and editing

Jean-Benoit: providing material, technical support, industrial application, reviewing, and editing

Data availability The datasets used in the current study are available from the corresponding author on reasonable request.

Code availability Not applicable.

Declarations

Ethics approval Not applicable.

Consent to participate Not applicable.

Consent for publication Not applicable.

Consent for publication All the authors have read and agreed to the published version of the manuscript.

Competing interests The authors declare no competing interests.

References

1. Bitterlin M, Loucif A, Charbonnier N, Jahazi M, Lapierre-Boire LP, Morin JB (2016) Cracking mechanisms in large size ingots of

high nickel content low alloyed steel. Eng Failure Anal 68. https://doi.org/10.1016/j.engfailanal.2016.05.027

2. Ren FC, Chen J, Chen F (2014) Constitutive modeling of hot deformation behavior of X20Cr13 martensitic stainless steel with strain effect. Trans Nonferrous Metals Soc China (Engl Ed) 24(5). https://doi.org/10.1016/S1003-6326(14)63206-4

3. B. Mahmoudi MJ, Torkamany AR, Aghdam S, Sabbaghzadeh J (2011) Effect of laser surface hardening on the hydrogen embrittlement of AISI 420: Martensitic stainless steel. Mater Des 32(5). https://doi.org/10.1016/j.matdes.2011.01.028

4. Sanrutsadakorn A, Uthaisangsuk V, Suranuntchai S, Thossatheppitak B (2012) Finite element modeling for hot forging process of AISI 4340 steel. Adv Mater Res 410. https://doi.org/10.4028/www.scientific.net/AMR.410.263

5. Chadha K, Shahriari D, Tremblay R, Bhattacharjee PP, Jahazi M (2017) Deformation and recrystallization behavior of the cast structure in large size, high strength steel ingots: experimentation and modeling. Metall Mater Trans A: Phys Metall Mater Sci 48(9). https://doi.org/10.1007/s11661-017-4177-8

6. Qin F, Zhu H, Wang Z, Zhao X, He W, Chen H (2017) Dislocation and twinning mechanisms for dynamic recrystallization of as-cast Mn18Cr18N steel. Mater Sci Eng A 684. https://doi.org/10.1016/j.msea.2016.12.095

7. Dimiduk DM, Martin PL, Kim YW (1998) Microstructure development in gamma alloy mill products by thermomechanical processing. Mater Sci Eng A 243(1–2). https://doi.org/10.1016/s0921-5093(97)00780-6

8. Tang B, Cheng L, Kou H, Li J (2015) Hot forging design and microstructure evolution of a high Nb containing TiAl alloy. Intermetallics (Barking) 58. https://doi.org/10.1016/j.intermet.2014.11.002

9. Marchattiwar A, Sarkar A, Chakravartty JK, Kashyap BP (2013) Dynamic recrystallization during hot deformation of 304 austenitic stainless steel. J Mater Eng Perform 22(8). https://doi.org/10.1007/s11665-013-0496-0

10. McQueen HJ, Jonas JJ (1975) Recovery and recrystallization during high temperature deformation. Plast Deform of Mater. https://doi.org/10.1016/b978-0-12-341806-7.50014-3

11. Jonas JJ, Poliak EI (2003) The critical strain for dynamic recrystallization in rolling mills, in Materials Science Forum, vol. 426–432(1). https://doi.org/10.4028/www.scientific.net/msf.426-432.57

12. Ebrahimi GR, Keshmiri H, Maldad AR, Momeni A (2012) Dynamic recrystallization Behavior of 13%Cr martensitic stainless steel under hot working condition. J Mater Sci Technol 28(5). https://doi.org/10.1016/S1005-0302(12)60084-X

13. Xiao W, Wang B, Wu Y, Yang X (2018) Constitutive modeling of flow behavior and microstructure evolution of AA7075 in hot tensile deformation. Mater Sci Eng A 712. https://doi.org/10.1016/j.msea.2017.12.028

14. Gao P, Fu M, Zhan M, Lei Z, Li Y (2020) Deformation behavior and microstructure evolution of titanium alloys with lamellar microstructure in hot working process: a review. J Mater Sci Technol 39. https://doi.org/10.1016/j.jmst.2019.07.052

15. Gao P, Zhan M, Fan X, Lei Z, Cai Y (2017) Hot deformation behavior and microstructure evolution of TA15 titanium alloy with nonuniform microstructure. Mater Sci Eng A 689. https://doi.org/10.1016/j.msea.2017.02.054

16. Goetz RL, Semiatin SL (2001) The adiabatic correction factor for deformation heating during the uniaxial compression test. J Mater Eng Perform 10(6). https://doi.org/10.1361/105994901770344593

17. Ye Xj, Gong Xj, Yang Bb, Li Yp, Nie Y (2019) Deformation inhomogeneity due to sample–anvil friction in cylindrical compression test. Trans Nonferrous Metals Soc China (Engl Ed) 29(2). https://doi.org/10.1016/S1003-6326(19)64937-X

18. Han Y, Qiao G, Sun J, Zou D (2013) A comparative study on constitutive relationship of as-cast 904L austenitic stainless steel during hot deformation based on Arrhenius-type and artificial neural network models. Comput Mater Sci 67. https://doi.org/10.1016/j.commatsci.2012.07.028

19. Samantaray D, Mandal S, Borah U, Bhaduri AK, Sivaprasad Pv (2009) A thermo-viscoplastic constitutive model to predict elevated-temperature flow behaviour in a titanium-modified austenitic stainless steel. Mater Sci Eng A 526(1–2). https://doi.org/10.1016/j.msea.2009.08.009

20. Ivaniski TM, Epp J, Zoch HW, da Silva Rocha A (2019) Austenitic grain size prediction in hot forging of a 20mncr5 steel by numerical simulation using the JMAK model for industrial applications. Mater Res 22(5). https://doi.org/10.1590/1980-5373-MR-2019-0230

21. Yeom JT, Kim JH, Park NK, Choi SS, Lee CS (2007) Ring-rolling design for a large-scale ring product of Ti-6Al-4V alloy. J Mater Process Technol 187–188. https://doi.org/10.1016/j.jmatprotec.2006.11.042

22. Srinivasan N, Prasad YVRK, Rama Rao P (2008) Hot deformation behaviour of Mg-3Al alloy-a study using processing map. Mater Sci Eng A 476(1–2). https://doi.org/10.1016/j.msea.2007.04.103

23. Pu P, Zheng W, Xiang J, Song Z, Li J (2014) Hot deformation characteristic and processing map of superaustenitic stainless steel S32654. Mater Sci Eng A 598. https://doi.org/10.1016/j.msea.2014.01.027

24. Babu KA, Mandal S, Athreya CN, Shakthipriya B, Sarma VS (2017) Hot deformation characteristics and processing map of a phosphorous modified super austenitic stainless steel. Mater Des 115. https://doi.org/10.1016/j.matdes.2016.11.054

25. Venugopal S, Mannan SL, Prasad YVRK (1992) Processing map for cold and hot working of stainless steel type AISI 304 L. Mater Lett 15(1–2). https://doi.org/10.1016/0167-577X(92)90016-D

26. Chegini M, Aboutalebi MR, Seyedein SH, Ebrahimi GR, Jahazi M (2020) Study on hot deformation behavior of AISI 414 martensitic stainless steel using 3D processing map. J Manuf Process 56. https://doi.org/10.1016/j.jmapro.2020.05.008

27. Zhou X, Ma W, Feng C, Zhang L (2020) Flow stress modeling, processing maps and microstructure evolution of 05Cr17Ni4Cu4Nb martensitic stainless steel during hot plastic deformation. Mater Res Express 7(4). https://doi.org/10.1088/2053-1591/ab89d8

28. Chen F, Ren F, Chen J, Cui Z, Ou H (2016) Microstructural modeling and numerical simulation of multi-physical fields for martensitic stainless steel during hot forging process of turbine blade. Int J Adv Manuf Technol 82(1–4). https://doi.org/10.1007/s00170-015-7368-8

29. Saksala T (2019) Numerical modeling of adiabatic heat generation during rock fracture under dynamic loading. Int J Numer Anal Methods Geomech 43(9). https://doi.org/10.1002/nag.2935

30. Nasraoui M, Forquin P, Siad L, Rusinek A (2012) Influence of strain rate, temperature and adiabatic heating on the mechanical behaviour of poly-methyl-methacrylate: experimental and modelling analyses. Mater Des 37. https://doi.org/10.1016/j.matdes.2011.11.032

31. Li S, Li L, He H, Wang G (2019) Influence of the deformation heating on the flow behavior of 6063 alloy during compression at medium strain rates. J Mater Res 34(2). https://doi.org/10.1557/jmr.2018.367

32. Castellanos J, Rieiro I, Cars M, Muoz J, Ruano OA (2007) Analysis of adiabatic heating in high strain rate torsion tests by an iterative method: application to an ultrahigh carbon steel, in WIT Transactions on Engineering Sciences, vol. 57. https://doi.org/10.2495/MC070221

33. Li YP, Onodera E, Matsumoto H, Chiba A (2009) Correcting the stress-strain curve in hot compression process to high strain level. Metall Mater Trans A: Phys Metall Mater Sci 40(4). https://doi.org/10.1007/s11661-009-9783-7

34. Hansel A, Spittel T (1978) Kraft- und Arbeitsbedarf bildsamer Formgeburgsverfahren.Leipzig. VEB DeutscherVerlag fur Grundstoffindustrie

35. Liang Q, Liu X, Li P, Ding P, Zhang X (2020) Development and application of high-temperature constitutive model of hni55–7–4–2 alloy. Metals (Basel) 10(9). https://doi.org/10.3390/met10091250

36. Sellars CM, McTegart WJ (1966) On the mechanism of hot deformation. Acta Metall 14(9).https://doi.org/10.1016/0001-6160(66)90207-0

37. McQueen HJ, Ryan ND (2002) Constitutive analysis in hot working. Mater Sci Eng A 322(1–2). https://doi.org/10.1016/S0921-5093(01)01117-0

38. Jabbari Taleghani MA, Ruiz Navas EM, Salehi M, Torralba JM (2012) Hot deformation behaviour and flow stress prediction of 7075 aluminium alloy powder compacts during compression at elevated temperatures. Mater Sci Eng A 534. https://doi.org/10.1016/j.msea.2011.12.019

39. Lin YC, Chen MS, Zhang J (2009) Modeling of flow stress of 42CrMo steel under hot compression. Mater Sci Eng A 499(1–2). https://doi.org/10.1016/j.msea.2007.11.119

40. Zhou Z et al (2017) Constitutive relationship and hot processing maps of Mg-Gd-Y-Nb-Zr alloy. J Mater Sci Technol 33(7). https://doi.org/10.1016/j.jmst.2015.10.019

41. Ashtiani HRR, Shahsavari P (2016) Strain-dependent constitutive equations to predict high temperature flow behavior of AA2030 aluminum alloy. Mech Mater 100. https://doi.org/10.1016/j.mechmat.2016.06.018

42. Anoop CR, Prakash A, Giri SK, Narayana Murty SVS, Samajdar I (2018) Optimization of hot workability and microstructure control in a 12Cr-10Ni precipitation hardenable stainless steel: an approach using processing maps. Mater Charact 141. https://doi.org/10.1016/j.matchar.2018.04.025

43. Samantaray D, Mandal S, Bhaduri AK (2009) A comparative study on Johnson Cook, modified Zerilli-Armstrong and Arrhenius-type constitutive models to predict elevated temperature flow behaviour in modified 9Cr-1Mo steel. Comput Mater Sci 47(2). https://doi.org/10.1016/j.commatsci.2009.09.025

44. Rao KP, Prasad YVRK, Suresh K (2011) Hot working behavior and processing map of a γ-TiAl alloy synthesized by powder metallurgy. Mater Des 32(10). https://doi.org/10.1016/j.matdes.2011.06.003

45. Prasad YVRK, Rao KP, Sasidhara S (2015) Hot working guide: a compendium of processing maps

46. Kim WJ, Jeong HT (2020) Easy construction of processing maps for metallic alloys using a flow instability criterion based on power-law breakdown. J Mater Res Technol 9(3): https://doi.org/10.1016/j.jmrt.2020.03.030

47. Ziegler H, Sneedon IN, Hill R (Eds.) (1963) Progress in solid mechanics. Wiley, New York, pp. 63–193